Oxygen-vacancy complex in silicon. I. ^{29}Si electron-nuclear double resonance

R. van Kemp, E. G. Sieverts, and C. A. J. Ammerlaan
Natuurkundig Laboratorium der Universiteit van Amsterdam, Valckenierstraat 65, NL-1018 XE Amsterdam, The Netherlands
(Received 26 January 1989)

The negative charge state of the oxygen-vacancy complex in silicon has been studied by electron-nuclear double resonance. Hyperfine interactions between the unpaired electron and ^{29}Si nuclei in 50 shells of neighboring lattice sites have been determined. These shells contain 145 lattice sites. From a linear combination of atomic orbitals analysis, it was deduced that the defect wave function was primarily localized on silicon atoms in a single ⟨011⟩ lattice chain that contains the vacant lattice site. The same preference for a one-dimensional extent of the wave function had already been observed in the single vacancy in silicon. As for the vacancy, a symmetry-forbidden plane of lattice sites is observed for the vacancy-oxygen complex as well. In addition to the hyperfine interactions that could be identified with lattice sites in the chain or in the forbidden plane, many more hyperfine interaction counterparts could be identified from the results for the vacancy. Since for a total of 66% of all interactions a correspondence between the oxygen-vacancy complex and the vacancy was found to exist, it is concluded that the electronic structures of both defects are highly similar.

I. INTRODUCTION

A. General

The first paramagnetic center observed in silicon that was irradiated at room temperature with electrons at an energy of about 1 MeV was called the A center. Later, when a more systematic nomenclature was introduced, this electron-paramagnetic-resonance (EPR) spectrum was named the Si-$B1$ spectrum. From experiments by Bemski[1] and by Watkins *et al.*,[2] it followed that the defect could only be detected in irradiated, oxygen-containing n-type silicon. The atomic model deduced from these data is that of a vacancy that is trapped by an interstitial oxygen atom. The defect is paramagnetic in its negatively charged state, O-V^-. This model was substantiated by the symmetry of the defect, which is point group $2mm$, and the resolved hyperfine interaction with two ^{29}Si nuclei. Furthermore, after irradiation at low temperature ($T<20$ K), other paramagnetic centers were observed, one of which was later identified as the negative isolated vacancy.[3,4] Under these circumstances, spectrum $B1$ is present only after annealing at temperatures above 70 K, the temperature at which the negative vacancies become mobile. This latter observation is strong support for the explanation of the formation process of the oxygen-vacancy complex.

Hyperfine interactions which are unresolved in EPR can often be resolved with electron-nuclear double resonance (ENDOR). Such studies have been performed on a number of vacancy-related defects—among others, both paramagnetic charge states of the divacancy[5,6] and the negatively charged single vacancy V^-.[7,8] Hyperfine interactions with large numbers of surrounding ^{29}Si nuclei have been determined in this way. A rationale to perform the present ENDOR experiment was the observed similarities between V^- and O-V^-: (1) both centers have the same symmetry, (2) the g tensors of both defects are very similar, and (3) the largest hyperfine interactions, ascribed to the nearest silicon neighbors, have the same symmetry and are nearly equal. The present ENDOR experiment will show that on a microscopic scale both defects exhibit many more striking and, therefore, most interesting similarities. Throughout this paper we will therefore compare results for O-V^- with those obtained for V^-. In Table I the data obtained by EPR for both defects are given. Figure 1 shows the models for both defects.

The core of the oxygen-vacancy complex, the oxygen atom, constitutes the major structural difference with the vacancy. This structural difference must be the origin of the considerable difference between the dynamic properties of the two defects. Hyperfine interactions with the ^{17}O nucleus, determined in samples especially enriched in this isotope, are discussed in the following paper.[9]

B. Electronic structure of the oxygen-vacancy complex

As the paramagnetism of the defect arises from a single unpaired electron, we will describe the electronic structure of the oxygen-vacancy complex using a one-electron model, the simplest being a linear combination of atomic orbitals (LCAO) approach. Such a wave function can be constructed from orbitals centered on the four silicon ligands a, b, c, and d (Fig. 1).

In cubic symmetry (point group $\bar{4}3m$)—thus actually for a substitutional oxygen atom—the electronic levels are of a_1 or t_2 symmetry. The a_1 levels, constituted by the $(a+b+c+d)$ combination of ligand orbitals, can accommodate two electrons; the t_2 levels, from the $(a-b-c+d)$, $(a+b-c-d)$, and $(a-b+c-d)$ combinations, can accommodate six electrons. The energy-level diagram for the oxygen-vacancy complex in $\bar{4}3m$ symmetry is shown in Fig. 2. In the negative charge

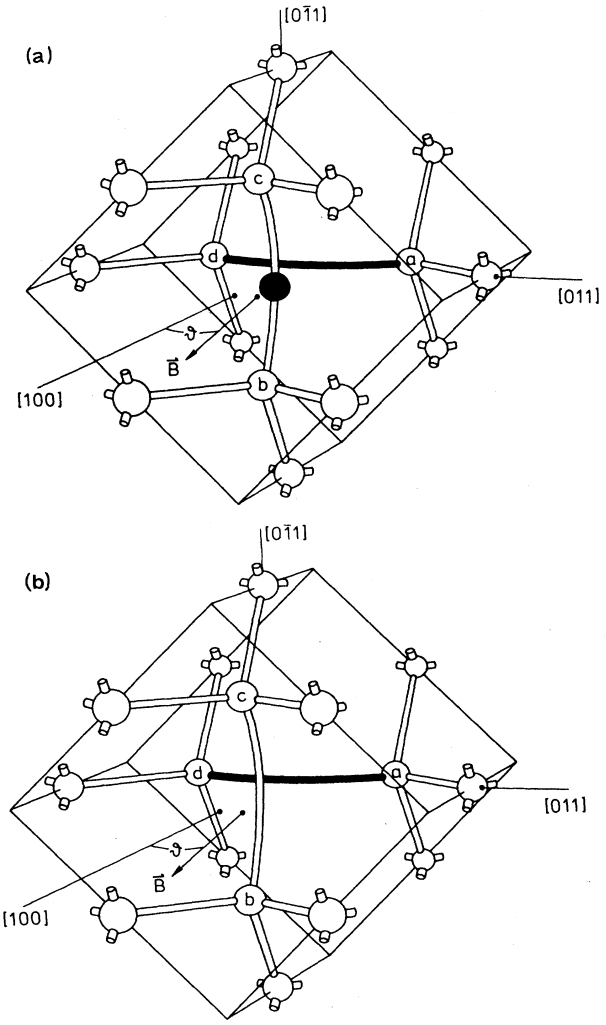

FIG. 1. Models of (a) the negative oxygen-vacancy and (b) the negatively charged vacancy. Shown are the defects in the standard orientation *ad*. The oxygen atom is represented by the solid sphere.

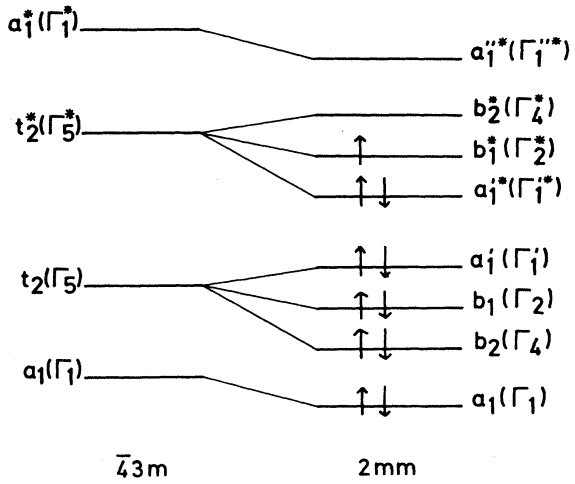

FIG. 2. Possible level scheme for the negatively charged state of the oxygen-vacancy complex in silicon. The symmetry is lowered from $\bar{4}3m$ to $2mm$ by Jahn-Teller distortion, lifting the degeneracy of the t_2 level. Levels are labeled according to the irreducible representations to which they belong.

state, 11 electrons occupy the various levels. The lowest levels can accommodate eight electrons in bonding orbitals between the oxygen atom and nearest-neighbor silicon atoms. The remaining three electrons have to be placed in antibonding levels. The lowest of these is the threefold orbitally degenerate t_2 level. By two successive Jahn-Teller distortions, the symmetry will be lowered from cubic to rhombic I (point group $2mm$). The unpaired electron occupies the b_1^* level. This antibonding level is experimentally found at 0.17 eV below the conduction band.[1] The wave function of this electron can be written as $(a-d)$. This implies a strong localization on the ligands a and d.

The EPR measurements of Watkins and Corbett[10] confirmed that this is a good approximation, as from their measurements it followed that 70% of the defect electron is centered at these atoms. Another consequence of this description is that the wave function is antisymmetric with respect to reflection about the (011) mirror plane and rotation about the twofold axis. This is reflected in the hyperfine interactions with atoms in this plane and on this axis. This will be discussed in Sec. III B.

C. The spin Hamiltonian

The oxygen-vacancy complex in its singly negative charge state has point-group symmetry $2mm$ and electron spin $S=\frac{1}{2}$. The EPR measurements can be described with the spin Hamiltonian

$$\mathcal{H}=\mu_B \mathbf{B}\cdot\vec{\mathbf{g}}\cdot\mathbf{S}\ , \tag{1}$$

which accounts for the interaction between the unpaired defect electron and the magnetic field. The symmetry of the defect puts constraints on the elements of the $\vec{\mathbf{g}}$ tensor

TABLE I. g values of the negatively charged oxygen-vacancy complex and the negative vacancy (Refs. 10 and 4). Also, thermal-annealing characteristics are included.

Spectrum	Model	Point-group symmetry	g values $g_{1,\parallel\langle 100\rangle}$	$g_{2,\parallel\langle 011\rangle}$	$g_{3,\parallel\langle 0\bar{1}1\rangle}$	Annealing temperature (K)
Si-*B*1	O-V^-	$2mm$	2.0031	2.0025	2.0093	720
Si-*G*2	V^-	$2mm$	2.0038	2.0028	2.0151	60

if written in Cartesian coordinates: $g_{yy}=g_{zz}$ and $g_{xy}=g_{xz}=0$.

In an ENDOR experiment hyperfine interactions of the unpaired defect electron with magnetic ^{29}Si nuclei in the lattice are determined. Therefore, terms are added to the spin Hamiltonian that describe this interaction and the nuclear Zeeman interaction. The spin Hamiltonian then reads

$$\mathcal{H}=\mu_B \mathbf{B}\cdot\overleftrightarrow{g}\cdot\mathbf{S}+\sum_i (\mathbf{S}\cdot\overleftrightarrow{A}_i\cdot\mathbf{I}_i-g_N\mu_N\mathbf{B}\cdot\mathbf{I}_i) , \quad (2)$$

with $S=\frac{1}{2}$ and $I_i=\frac{1}{2}$. The label i enumerates the atom sites surrounding the defect.

The addition of a magnetic ^{29}Si nucleus to the defect puts constraints on the form of the tensor $\overleftrightarrow{A}_i$, depending on the position of the ^{29}Si nucleus. Silicon atoms that occupy symmetry-equivalent sites form a so-called shell of atoms. One can distinguish four cases.

(1) The ^{29}Si atom is on a general lattice site $[xyz]$. Transformations of the point group, i.e., E, $m_{(011)}$, $m_{(0\bar{1}1)}$, and $2_{[100]}$, generate four different positions in the shell, $[xyz]$, $[x\,\bar{z}\,\bar{y}]$, $[xzy]$, and $[x\,\bar{y}\,\bar{z}]$, respectively. Hyperfine tensors of this kind are called general class tensors and are labeled G.

(2) The ^{29}Si nucleus lies in the $(0\bar{1}1)$ plane. Positions in a shell are $[xyy]$ and $[x\,\bar{y}\,\bar{y}]$. As hyperfine tensors of this kind describe the hyperfine interactions with nuclei that lie in the same mirror plane as the atoms a and d in Fig. 1, they are called *Mad* tensors.

(3) The ^{29}Si nucleus lies in the (011) plane. Positions in a shell are $[x\bar{y}y]$ and $[xy\bar{y}]$. As hyperfine tensors of this kind are associated with sites in the same mirror plane as the atoms b and c in Fig. 1, they are called *Mbc*-class tensors.

(4) The ^{29}Si nucleus lies on the [100] axis through the defect. There is only one position, $[x00]$, in each shell. A tensor for lattice sites of this kind is called a twofold-axis-class tensor; the label is T.

The first-order solution of the spin Hamiltonian [Eq. (2)] for a particular shell i is

$$E=\mu_B g_{\text{eff}} B m_S+m_S m_I A_{\text{eff}}-g_N\mu_N B m_I . \quad (3)$$

EPR transitions are those where $\Delta m_S=\pm 1$ and $\Delta m_I=0$; ENDOR (NMR) transitions are those where $\Delta m_S=0$ and $\Delta m_I=\pm 1$. From Eq. (3) it follows that the ENDOR frequencies will be found at

$$\Delta E=h\nu=|g_N\mu_N B\pm\tfrac{1}{2}A_{\text{eff}}| . \quad (4)$$

The frequency $\nu_z=|g_N\mu_N B/h|$ is called the nuclear Zeeman frequency. Equation (4) shows that, to first order, the ENDOR frequencies will be found symmetrically below and above the nuclear Zeeman frequency.

D. LCAO analysis

The experimentally found hyperfine tensors $\overleftrightarrow{A}$ are related to the wave function of the defect electron in the crystal. It is often a good approximation to write the wave function as a linear combination of silicon $3s$ and $3p$ orbitals. This approximation has shown to be very useful in describing vacancy-related defects.

The wave function centered at an atomic site i is thus written as

$$\phi_i=\alpha_i s_i+\beta_i\phi_{3p,i} , \quad (5)$$

with the normalization constraint $\alpha_i^2+\beta_i^2=1$. The whole wave function is the sum over all lattice sites i,

$$\Psi=\sum_i \eta_i\phi_i , \quad (6)$$

where η_i^2 is the localization of the defect electron on site i.

We will now calculate the symmetrized orbitals ϕ_i for the b_1^* level for the four different classes of shells. We start with an sp-hybrid orbital centered at site j of the shell. The index $j=1$–4 enumerates the sites in a shell following $j=1$, $[xyz]$; $j=2$, $[xzy]$; $j=3$, $[x\,\bar{z}\,\bar{y}]$; and $j=4$, $[x\,\bar{y}\,\bar{z}]$:

$$\phi_j=\alpha s_j+\gamma x_j+\delta y_j+\epsilon z_j , \quad (7)$$

where x_j, y_j, and z_j are p orbitals along the x, y, and z directions. Using projection operators, we find the appropriate linear combinations of atomic orbitals for the b_1^* level. For the general-class shell,

$$\phi_i=\tfrac{1}{4}\alpha_i(s_1+s_2-s_3-s_4)+\tfrac{1}{4}\gamma_i(x_1+x_2-x_3-x_4)$$
$$+\tfrac{1}{4}\delta_i(y_1+z_2+z_3+y_4)+\tfrac{1}{4}\epsilon_i(z_1+y_2+y_3+z_4) . \quad (8)$$

For the $(0\bar{1}1)$-mirror-plane–class shell, we have

$$\phi_i=\tfrac{1}{2}\alpha_i(s_1-s_3)+\tfrac{1}{2}\gamma_i(x_1-x_3)$$
$$+\tfrac{1}{4}(\delta_i+\epsilon_i)(y_1+y_3+z_1+z_3) . \quad (9)$$

For the (011)-mirror-plane–class shell, we have

$$\phi_i=\tfrac{1}{4}(\delta_i+\epsilon_i)(y_1+y_2+z_1+z_2) , \quad (10)$$

and for the twofold-axis-class shell,

$$\phi_i=\tfrac{1}{2}(\delta_i+\epsilon_i)(y_1+z_1) . \quad (11)$$

This means that, at general-class lattice sites, admixture of s orbitals and of p orbitals in arbitrary directions is allowed. On sites in the $(0\bar{1}1)$ mirror plane, p orbitals parallel to the plane and s orbitals are allowed. On the (011) mirror plane, symmetry restricts to p orbitals along [011], perpendicular to the plane, just as for sites on the twofold axis, while s orbitals are forbidden.

The hyperfine-interaction term $\mathbf{S}\cdot\overleftrightarrow{A}\cdot\mathbf{I}$ can be calculated from the relation $\mathbf{S}\cdot\overleftrightarrow{A}\cdot\mathbf{I}=\langle\Psi|\mathcal{H}_{\text{hf}}|\Psi\rangle$, where $\mathcal{H}_{\text{hf}}$ is the hyperfine-interaction operator. When we neglect contributions other than those from the orbitals centered at the site i, assuming that the overlap is vanishingly small, and do not correct for distant dipole-dipole interactions, this results in expressions for the hyperfine-interaction tensors $\overleftrightarrow{A}_i$ that can be written as

$$\overleftrightarrow{A}_i=a_i\overleftrightarrow{1}+\overleftrightarrow{B}_i . \quad (12)$$

The first term is the isotropic Fermi-contact interaction,

$$a_i=\tfrac{2}{3}\mu_0 g\mu_B g_N\mu_N\eta_i^2\alpha_i^2|\Psi(0)|_s^2 . \quad (13)$$

The second term is the anisotropic dipole-dipole interaction,

$$B_{lm}(i)=\frac{\mu_0}{4\pi}g\mu_B g_N\mu_N\left\langle\Psi\left|\frac{3x_1x_m}{r^5}-\frac{\delta_{lm}}{r^3}\right|\Psi\right\rangle . \quad (14)$$

Inserting expressions (8)–(11) into Eq. (14) gives the dipole-dipole–interaction tensor $\overleftrightarrow{B}_i$ with principal values $(2b_i,-b_i,-b_i)$, where

$$b_i=\frac{2}{5}\frac{\mu_0}{4\pi}g\mu_B g_N\mu_N\eta_i^2\beta_i^2\langle r^{-3}\rangle_p , \quad (15)$$

with $\beta_i^2=\gamma_i^2+\delta_i^2+\epsilon_i^2$ the total amount of p character. The atomic wave-function parameters can be obtained from theoretical calculations. We will use values that Morton and Preston[11] derived from Hartree-Fock-Slater atomic orbitals by Herman and Skillman, $|\Psi(0)|_s^2=34.52\times10^{30}$ m^{-3} and $\langle r^{-3}\rangle_p=18.16\times10^{30}$ m^{-3}.

This analysis thus gives a purely axial hyperfine tensor $\overleftrightarrow{A}$. For the present point-group symmetry, experimental hyperfine tensors need not be axial, however, and therefore principal values of $\overleftrightarrow{A}$ can be written as

$$(a_i+2b_i,\ a_i-b_i+c_i,\ a_i-b_i-c_i) , \quad (16)$$

where c_i gives an indication about the deviation from the axial form.

II. EXPERIMENT

A. Sample preparation

In order to obtain the highest possible concentration of oxygen-vacancy complexes, oxygen was diffused into 0.025-Ω cm float-zone phosphorus-doped n-type silicon ([P]$=9\times10^{17}$ cm^{-3}). Float-zone silicon was used instead of crucible-grown silicon because the latter material was not available with sufficiently high phosphorus concentration.

Samples (dimensions $2\times2\times20$ mm^3) were first oxidized by heating them for 16 h at 1200 °C in a closed quartz ampoule in which a few milligrams of water were put prior to the heating. The oxidized samples were then enclosed in another quartz ampoule and heated for 10 d at 1390 °C. This was sufficiently long to obtain a homogeneous oxygen concentration. Samples were then slowly cooled down and ground to remove the surface layer. This procedure minimizes the risk of breaking the samples during the final quench, as a surface layer of SiO_2 and/or Si_2N_3 has a low thermal conduction and thus causes mechanical strains. Finally, samples were heated to about 1350 °C for a few hours. Then they were quenched in about 2 min to room temperature. This relatively slow quench has the result that fast-diffusing elements, such as inevitably present transition metals, have time to cluster to nonparamagnetic centers.

Electron irradiations were done with a Van De Graaff electrostatic accelerator. Typical energies and dose rates for the production of the $B1$ center were 1.5 MeV and 4 μA cm^{-2}. Samples were mounted on a copper block in a holder with a water-cooled mantle. During the irradiations the temperature of the samples was kept below 70 °C.

Because of the high phosphorus concentration, phosphorus-vacancy complexes and other phosphorus-related spectra will also be produced during the irradiations.[12–14] The production and presence of other defects means that less O-V^- complexes are formed. As the oxygen-vacancy complex has the highest annealing temperature of most of the produced defects, samples were annealed for about 15 min at 220 °C after irradiation. In this process nearly all vacancy-related defects except O-V^- dissociate. The mobile vacancies produced are captured by interstitial oxygen atoms and create additional oxygen-vacancy complexes. The irradiation–annealing–EPR experiment cycle was repeated a few times until a high enough intensity of the $B1$ spectrum was obtained.

B. Experimental setup

EPR and ENDOR experiments were performed in a cryostat that was originally designed for an ENDOR experiment on the single vacancy in silicon. A detailed description of this cryostat can be found in Ref. 15. Although designed to perform low-temperature electron irradiations as well, this cryostat was used because of its low helium consumption at the measurement temperature of about 25 K, its capability of unattended operation for periods up to 36 h, and its proven reliability over long periods of operation.

A K-band superheterodyne spectrometer was used. Detailed descriptions of this spectrometer can be found in Refs. 14 and 15. For the ENDOR experiments a cylindrical TE_{011}-resonance cavity was used. It was made of Epibond with a silvered inner wall in which a spiral groove was cut, so that it acts as a rf coil.[16]

The magnetic field was measured by a Bruker B-NM20 proton resonator. The value of the field as measured is fed into a microprocessor that controls the magnetic field with an accuracy of ±2 μT, by means of a program written in FORTH. Various programs for the magnetic field can be run, for instance, to shift the magnetic field in a linear relation with the applied radiofrequency during an ENDOR experiment, in order to induce EPR transitions in the right spin packets.

ENDOR signals were recorded as changes in the dispersion component of the EPR signal using double phase-sensitive detection. The magnetic field was sine-wave modulated with a frequency of 83.3 Hz and the rf was on-off modulated with a frequency of 3.3 Hz.

C. Experimental results

In exploratory EPR measurements the g tensor of the $B1$ center was determined by a computer fit. The calculated principal values of the $\overleftrightarrow{g}$ tensor were $g_{1,\parallel\langle100\rangle}=2.0033\pm0.0001$, $g_{2,\parallel\langle011\rangle}=2.0025\pm0.0001$, and $g_{3,\parallel\langle0\bar{1}1\rangle}=2.0093\pm0.0001$, in close agreement with the values given by Watkins and Corbett (Table I). Figure 3 shows a plot of the angular dependence of the effective g value, g_{eff}, with the magnetic field in the $(0\bar{1}1)$ plane, and as a function of the angle with the [100] direction. The four different curves are labeled according to Fig. 1. In

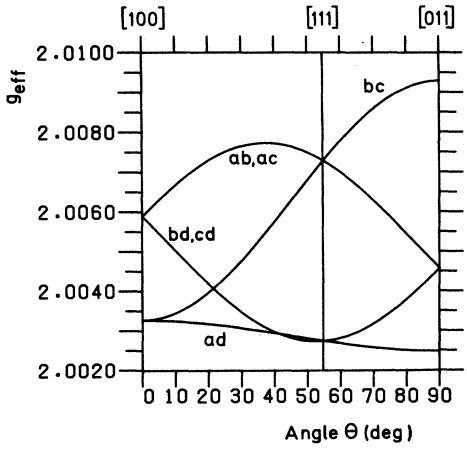

FIG. 3. Angular dependence of the effective g values for the oxygen-vacancy complex. The magnetic field is rotated in the (0$\bar{1}$1) plane. The different orientations are labeled in accordance with Fig. 1.

principle, there are six different orientations, but when measuring in a symmetry plane of the defect, the resonances of the orientations *ab* and *ac* and those of *bd* and *cd* coincide.

In most cases, ENDOR measurements were performed on a single transition, i.e., only frequencies in the range $\nu > \nu_z$ were scanned. Angle-dependent rf scans were only made for the EPR orientations *ad* and *bc*. For frequencies $\nu - \nu_z < 1.5$ MHz, they were made at 10° intervals, and at $\nu - \nu_z < 300$ kHz, even at 5° or 2° intervals, as necessitated by overlap of the patterns. This overlap is, in fact, the main limitation to the smallest hyperfine-interaction tensor that can still be analyzed. Another limitation is the fact that for angles where two EPR lines come close together, it cannot be decided which ENDOR lines belong to which EPR line and, thus, to which orientation. This made it impossible to do measurements on orientation *ad* between 35° and 65°. Figure 4 shows a part of a recorded ENDOR spectrum with high resolution.

All the measured hyperfine tensors were determined by making computer fits to the spin Hamiltonian [Eq. (2)]. In these fits the electronic g values and the nuclear g value, g_N, were kept constant at their previously determined values. The nuclear g value was determined by measuring the frequencies of both ENDOR transitions for the tensor *Mbc*3. Making a computer fit with g_N as a free parameter as well, we found $|g_N| = 1.1096 \pm 0.0001$, in good agreement with literature.[17] In general, only points measured in the three directions of high symmetry were used for the computer fits. Angle-dependent patterns for orientations *ad* and *bc* were only used to sort out which high-symmetry points belonged to the same hyperfine tensor, and to determine the symmetry of the pertinent shell of lattice sites.

We measured the hyperfine interactions with 50 shells of silicon atoms: 23 *G*-class tensors, 20 *Mad*-class tensors, 6 *Mbc*-class tensors, and only one *T*-class tensor. These 50 shells contain 145 atoms. Principal values of the 50 hyperfine-interaction tensors are given in Table II together with the principal directions expressed in the angle γ_i between the direction of the principal axes and the (0$\bar{1}$1) plane and the angle δ_i between the projection on this plane and the [100] direction. The linewidths of the ENDOR lines are between 1 and 3 kHz for most of the interactions. For the interactions *G*1-*G*4, *G*10, and *Mad*3-*Mad*7 the linewidths are between 8 and 15 kHz, and for *Mad*2 70 kHz and for *Mad*1 300 kHz. The experimental uncertainty in the determined values is, in general, 10% of the linewidth.

Table III gives the reduced hyperfine parameters a, b, and c, and the LCAO parameters α^2, β^2, and η^2, which are calculated using expressions (13)–(16), and $\alpha^2 + \beta^2 = 1$. As it is not possible to determine the absolute signs of a and b from experiment, we always choose $a > 0$. In some

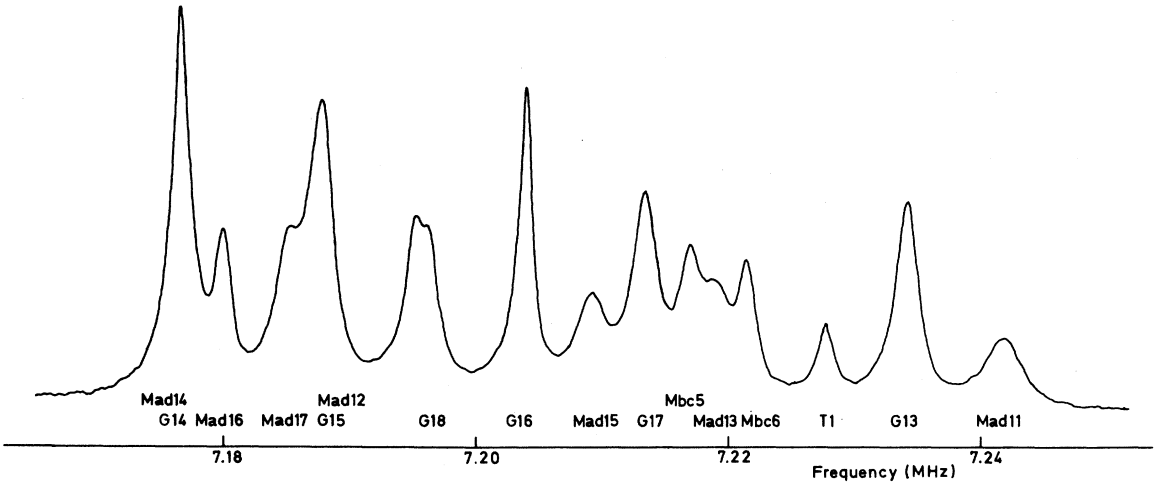

FIG. 4. ENDOR scan with very high resolution with the magnetic field **B**||[100] for the orientations *ad* and *bc*. The tensors are labeled according to Table II. The microwave frequency was $\nu_m = 23.2922$ GHz and the scan speed was 58.4 kHz/h.

cases this led to $b<0$. In view of the coefficients in Eqs. (13) and (15), a LCAO description requires a and b of equal (and actually negative) signs. From Eq. (16), c also was calculated; b and c are chosen such that $|b|>|c|$. Also, the quotients a/b and b/c are given. They give an indication about the anisotropy and the deviation from axiality, respectively. If we choose the value $|b/c|>5$ as a rather arbitrary criterion for the tensor to be "axial,"

TABLE II. Hyperfine parameters of the negatively charged oxygen-vacancy complex. Principal values A_i are given in kHz. γ_i is the angle of the ith principal direction with the $(0\bar{1}1)$ plane; δ_i is the angle between the projection of this direction on the $(0\bar{1}1)$ plane and the [100] direction. These figures refer to the EPR orientation *ad*. Experimental errors range from 60 kHz for *Mad*1 to 0.2 kHz for most of the smaller interactions.

Tensor	A_1	A_2	A_3	γ_1	δ_1	γ_2	δ_2	γ_3	δ_3
*G*1	20 520.9	14 599.5	14 364.2	−3.8	58.1	−30.9	−34.2	58.8	−25.6
*G*2	9789.6	7440.0	7293.9	−53.8	6.7	32.1	37.5	14.8	−62.0
*G*3	6840.8	6399.9	6134.3	49.7	83.2	−36.8	54.9	14.2	−24.2
*G*4	3832.1	2830.0	2760.9	−0.2	55.0	−29.8	−35.1	60.2	−34.7
*G*5	2324.7	1662.1	1638.4	−55.5	8.8	31.5	35.7	12.6	−62.2
*G*6	1998.4	1650.2	1398.3	−66.1	28.4	23.8	33.1	1.7	−57.7
*G*7	1571.2	1438.7	1168.9	−38.6	26.7	51.4	30.9	2.0	−61.7
*G*8	1180.9	732.6	707.4	−8.6	60.4	−34.5	−35.5	54.1	−17.5
*G*9	976.7	768.2	748.8	−1.5	53.4	−29.0	−37.5	61.0	−33.9
*G*10	2108.8	1554.8	−1245.8	−28.7	−66.8	−17.2	32.9	55.7	−30.1
*G*11	761.0	570.4	567.0	−54.7	6.9	31.2	38.1	14.8	−61.1
*G*12	658.7	570.7	562.0	−37.7	25.7	−23.6	−84.0	43.1	−18.1
*G*13	543.2	388.0	368.5	−60.0	−6.4	4.5	75.8	29.6	−16.7
*G*14	415.9	311.8	297.6	−44.6	84.7	−45.1	−88.4	3.4	−1.9
*G*15	436.8	341.7	242.4	−69.1	53.2	19.0	27.8	−8.3	−59.3
*G*16	377.8	348.3	260.1	−51.5	21.8	37.8	9.2	−6.1	−76.0
*G*17	379.2	329.6	195.1	−5.9	21.7	6.8	−67.6	81.0	71.0
*G*18	549.7	394.9	−120.1	−56.9	−0.1	27.3	37.7	17.3	−61.6
*G*19	287.1	210.4	182.0	−44.8	84.4	0.4	−5.1	45.2	85.3
*G*20	250.6	229.4	192.5	−21.4	56.1	−53.3	−65.6	28.3	−21.8
*G*21	251.2	243.9	164.8	49.6	65.8	−34.8	30.6	17.9	−46.4
*G*22	267.8	221.2	149.4	60.0	78.3	−21.1	30.1	20.3	−51.7
*G*23	236.5	140.2	138.5	−5.5	70.1	−69.2	−34.6	20.0	−18.0
*Mad*1	460 437	389 614	387 377	0.0	53.8	90.0		0.0	−36.2
*Mad*2	47 567.9	35 846.1	34 765.8	0.0	51.6	90.0		0.0	−38.4
*Mad*3	31 796.6	23 589.9	22 963.0	0.0	48.5	90.0		0.0	−41.5
*Mad*4	20 439.9	16 306.3	16 001.2	0.0	51.5	90.0		0.0	−38.5
*Mad*5	7709.6	5798.5	5688.0	0.0	53.4	90.0		0.0	−36.6
*Mad*6	4084.5	3081.0	3021.6	0.0	51.6	90.0		0.0	−38.4
*Mad*7	3067.7	2735.8	2734.7	0.0	7.9	90.0		0.0	−82.1
*Mad*8	1908.1	1489.3	1456.0	0.0	52.9	90.0		0.0	−37.1
*Mad*9	1245.6	968.4	954.3	0.0	52.9	90.0		0.0	−37.1
*Mad*10	944.6	805.4	554.2	90.0		0.0	30.1	0.0	−59.9
*Mad*11	463.3	412.3	403.7	0.0	57.3	0.0	−32.7	90.0	
*Mad*12	756.1	300.3	212.9	0.0	80.5	0.0	−9.5	90.0	
*Mad*13	463.1	347.8	341.2	0.0	54.3	90.0		0.0	−35.7
*Mad*14	586.6	207.8	164.8	0.0	60.9	0.0	−29.1	90.0	
*Mad*15	524.2	220.2	206.1	0.0	45.5	90.0		0.0	−44.5
*Mad*16	456.2	243.0	240.8	0.0	57.5	0.0	−32.5	90.0	
*Mad*17	315.3	270.5	261.9	0.0	1.3	0.0	−88.7	90.0	
*Mad*18	303.4	235.1	229.8	0.0	53.5	90.0		0.0	−36.5
*Mad*19	241.2	180.4	180.2	0.0	52.3	0.0	−37.7	90.0	
*Mad*20	183.3	174.2	86.3	90.0		0.0	55.3	0.0	−34.7
*Mbc*1	2835.9	2302.7	2228.8	−40.5	0.0	49.5	0.0	0.0	90.0
*Mbc*2	1352.1	1188.6	1170.3	−40.8	0.0	0.0	90.0	49.2	0.0
*Mbc*3	1324.7	930.3	685.7	−23.4	0.0	0.0	90.0	66.7	0.0
*Mbc*4	1045.7	883.7	780.4	−68.6	0.0	21.4	0.0	0.0	90.0
*Mbc*5	412.9	334.2	308.5	−35.2	0.0	0.0	90.0	54.8	0.0
*Mbc*6	396.0	333.4	−474.4	5.6	0.0	0.0	90.0	−84.4	0.0
*T*1	697.8	597.8	401.6	90.0		0.0	90.0	0.0	0.0

then 12 of the 23 *G*-class tensors, 16 of the 20 *Mad*-class tensors, and 3 of the *Mbc*-class tensors can be called "axial." In practice, the distinction between axial and nonaxial tensors proves to be very useful, as only axial tensors comply with a pure LCAO analysis.

The localization η^2 of the defect electron is distributed as follows: *G* class, 24.20%; *Mad* class, 82.68%; *Mbc* class, 1.66%; *T* class, 0.084%—resulting in a total of

TABLE III. Reduced hyperfine parameters and calculated LCAO parameters of the oxygen-vacancy complex. Values of *a*, *b*, and *c* are in units of kHz. Fractions of *s* character α^2, *p* character β^2, and localization η^2 are calculated with the atomic wave-function parameters from Ref. 11, taking the absolute values of *a* and *b*. The suitability of the LCAO description is indicated by + or −. Assignment to lattice positions according to various model descriptions is given (see text).

Tensor	*a*	*b*	*c*	*a*/*b*	*b*/*c*	α^2	β^2	η^2 (%)	LCAO	Pos.	Model
*G*1	16494.9	2013.0	117.6	8.19	17.12	0.171	0.829	2.12	+	[$\bar{2}$24]	ch2
*G*2	8174.5	807.5	73.0	10.12	11.06	0.203	0.797	0.89	+	[$\bar{3}$35]	ch2
*G*3	6458.3	191.2	132.8	33.78	1.44	0.459	0.541	0.31	−		
*G*4	3141.0	345.5	34.6	9.09	9.99	0.186	0.814	0.37	+	[$\bar{4}$26]	ch2
*G*5	1875.1	224.8	11.8	8.34	19.05	0.173	0.827	0.24	+	[$\bar{5}$37]	ch2
*G*6	1682.3	158.0	125.9	10.65	1.25	0.211	0.789	0.24	−		
*G*7	1392.9	−112.0	−66.2	−12.44	1.69	0.238	0.762	0.13	−		
*G*8	873.7	153.6	12.6	5.69	12.19	0.125	0.875	0.15	+	[$\bar{6}$28]	ch2?
*G*9	831.2	72.7	9.7	11.43	7.49	0.223	0.777	0.08	+	[$\bar{6}$28]	ch2?
*G*10	805.9	−1025.9	−277.0	−0.79	3.70	0.019	0.981	0.92	−		
*G*11	632.8	64.1	1.7	9.87	37.71	0.199	0.801	0.07	+	[$\bar{7}$39]	ch2
*G*12	597.2	30.8	4.3	19.39	7.16	0.328	0.672	0.04	+		
*G*13	433.2	55.0	9.7	7.88	5.67	0.165	0.835	0.06	+		
*G*14	341.8	37.1	7.1	9.21	5.23	0.188	0.812	0.04	+	[$\bar{1}$15]	*dd*
*G*15	340.3	−49.0	−47.6	−6.94	1.03	0.149	0.851	0.05	−		
*G*16	328.7	−34.3	−14.8	−9.58	2.32	0.194	0.806	0.04	−		
*G*17	301.3	−53.1	−24.8	−5.67	2.14	0.125	0.875	0.05	−		
*G*18	274.8	−197.5	−77.4	−1.39	2.55	0.034	0.966	0.18	−		
*G*19	226.5	30.3	14.2	7.48	2.13	0.158	0.842	0.03	−		
*G*20	224.2	−15.8	−10.6	−14.19	1.49	0.263	0.737	0.02	−		
*G*21	220.0	−27.6	−3.6	−7.97	7.67	0.167	0.833	0.03	−		
*G*22	212.8	−31.7	−23.3	−6.71	1.36	0.144	0.856	0.03	−		
*G*23	171.8	32.4	0.9	5.30	36.00	0.118	0.882	0.03	+		
*Mad*1	412476.4	23980.4	1118.4	17.20	21.44	0.302	0.698	29.98	+	[$\bar{1}$11]	ch
*Mad*2	39393.3	4087.3	540.1	9.64	7.57	0.195	0.805	4.44	+	[022]	ch
*Mad*3	26116.5	2840.1	313.4	9.20	9.06	0.188	0.812	3.06	+	[$\bar{1}$33]	ch
*Mad*4	17582.5	1428.7	152.5	12.31	9.37	0.236	0.764	1.63	+	[044]	ch
*Mad*5	6398.7	655.4	55.3	9.76	11.85	0.197	0.803	0.71	+	[$\bar{1}$55]	ch
*Mad*6	3395.7	344.4	29.7	9.86	11.60	0.199	0.801	0.38	+	[066]	ch
*Mad*7	2846.1	110.8	0.6	25.69	184.67	0.392	0.608	0.16	+		
*Mad*8	1617.8	145.1	16.6	11.15	8.74	0.219	0.781	0.16	+	[$\bar{1}$77]	ch
*Mad*9	1056.1	94.7	7.1	11.15	13.34	0.219	0.781	0.11	+	[088]	ch
*Mad*10	768.1	−106.9	−69.6	−7.19	1.54	0.153	0.847	0.11	−		
*Mad*11	426.4	18.4	4.3	23.17	4.28	0.368	0.632	0.03	−		
*Mad*12	423.1	166.5	43.7	2.54	3.81	0.060	0.940	0.16	−		
*Mad*13	384.0	39.5	3.3	9.72	11.97	0.196	0.804	0.04	+	[$\bar{1}$99]	ch
*Mad*14	319.7	133.4	21.5	2.40	6.20	0.057	0.943	0.12	+		
*Mad*15	316.8	103.7	7.0	3.05	14.81	0.071	0.929	0.10	+		
*Mad*16	313.4	71.4	1.1	4.39	64.91	0.099	0.901	0.07	+		
*Mad*17	282.6	16.4	4.3	17.23	3.81	0.302	0.698	0.02	−		
*Mad*18	256.1	23.7	2.7	10.81	8.78	0.213	0.787	0.03	+	[0 10 10]	ch
*Mad*19	200.6	20.3	0.1	9.88	203.0	0.199	0.801	0.02	+		
*Mad*20	147.9	−30.8	−4.5	−4.80	6.84	0.108	0.892	0.03	−		
*Mbc*1	2455.8	190.1	37.0	12.92	5.14	0.245	0.755	0.22	+	[11$\bar{1}$]	*dd*
*Mbc*2	1237.0	57.6	9.1	21.48	6.33	0.350	0.650	0.08	+	[$\bar{4}\bar{2}$2]	*dd*
*Mbc*3	980.2	172.2	122.3	5.69	1.41	0.125	0.875	0.17	−	[$\bar{3}$ $\bar{1}$ 1]	*dd*
*Mbc*4	903.3	71.2	51.7	12.69	1.38	0.242	0.758	0.08	−	[0$\bar{2}\bar{2}$]	*dd*
*Mbc*5	351.9	30.5	12.9	11.54	2.36	0.225	0.775	0.03	−	[42$\bar{2}$]	*dd*
*Mbc*6	85.0	−279.7	−31.3	−0.30	8.94	0.008	0.992	0.25	−		
*T*1	565.7	−82.1	−50.0	−6.89	1.64	0.148	0.852	0.08	−	[$\bar{4}$00]	*dd*

TABLE IV. Comparison of the largest hyperfine interactions of O-V^-, as derived from an EPR experiment by Watkins and Corbett (Ref. 10) and from the present ENDOR experiment. Given are labels of the interactions, numbers n of pertinent lattice sites, and hyperfine parameters a and b in MHz.

Ref. 10				Present work			
Label	n	a	b	Label	n	a	b
A	2	410.4	24.3	*Mad*1	2	412.48	23.98
B	2	39.9	(3.9)	*Mad*2	2	39.393	4.087
C	2	26.4	(2.7)	*Mad*3	2	26.116	2.840
D	4–6	17.4	(1.8)	*Mad*4	2	17.582	1.428
				*G*1	4	16.495	2.013
E	4–6	7.5		*G*2	4	8.175	0.808
				*G*3	4	6.458	0.191
				*Mad*5	2	6.399	0.655

108.6%. If tensors without a proper LCAO behavior had been omitted from this analysis, a total localization of 99% is found.

In the original EPR experiment of Watkins and Corbett on O-V^-,[10] five more or less resolved hyperfine interactions have also been reported. These interactions, labeled A–E, can now easily be identified with the largest interactions from our present ENDOR experiment. The comparison in Table IV shows that the agreeement is very good, even though the anisotropy of the four smaller interactions could not be determined by EPR. The values for b shown in parentheses are only estimates, as given in Ref. 10. From Table IV we can see that the interactions D and E are actually superpositions of, respectively, two and three interactions. As these do not exactly coincide, the total numbers of atom sites they represent are, in fact, somewhat larger than Watkins and Corbett estimated from the intensities of their observed hyperfine satellites.

III. DISCUSSION

A goal of a ligand ENDOR experiment is often to assign hyperfine tensors to particular shells of silicon atoms. Unfortunately, so far no theoretical calculations and predictions exist for the hyperfine interactions of a deep-level defect electron with more than just a few surrounding silicon neighbors. On the basis of symmetry, tensors and sites can be assigned unambiguously to one of the four distinct classes, but when making assignments to sites within a class we are forced to rely on "proofs" of phenomenological nature. In the following we will discuss assignments of measured hyperfine tensors to specific shells of silicon atoms, largely in the same spirit as for the vacancy.[8]

To get some idea about the extension of the electronic wave function, in Fig. 5 the localizations η^2, as given in Table III, have been plotted as a function of the distance from the atoms in a shell to the center of the defect, under the assumption of monotonic decrease of the isotropic part. The solid lines are fits to the function

$$\eta(r)^2=\eta_0^2\exp(-r/r_0)\ . \tag{17}$$

Parameters η_0^2 and r_0 for three different symmetry types of neighbors are given in Table V. For comparison these parameters for V^- are reproduced as well.[8] The results for the G- and *Mad*-class tensors of O-V^- are very similar to V^-. The *Mbc* tensors show a rather pronounced difference. In view of the fact that only two of the six show a proper LCAO behavior, this may not be too significant. This presentation of the measured hyperfine tensors and the comparison with the results obtained for V^- is rather superficial, partly because it is based on somewhat unrealistic suppositions. In the following sections we will take a closer look at similarities.

A. The defect chain

As was noted by Sprenger *et al.*,[7,8,15] a group of the hyperfine tensors of the *Mad* class of V^- showed remark-

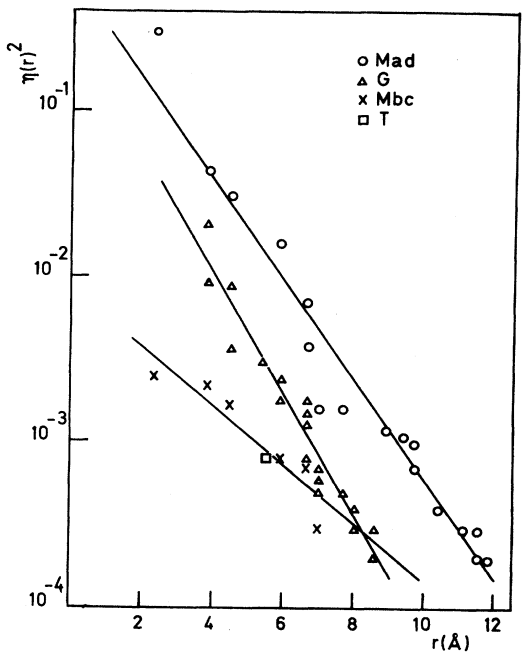

FIG. 5. Hyperfine interactions of the oxygen-vacancy complex, converted to values for the localization of the wave function, plotted against the distance from the center of the defect under the assumption of monotonic decrease. Solid lines are logarithmic fits to the function $\eta(r)^2=\eta_0^2\exp(-r/r_0)$, the parameters of which are shown in Table V.

TABLE V. Parameters for the fitted curves of Figs. 5 and 6. For comparison, the values for the same fits in the case of V^- (Ref. 8) are also given.

Defect	Shell type	η_0^2	r_0 (Å)
O-V^-	G	0.30	1.19
O-V^-	*Mad*	0.62	1.44
O-V^-	$Mbc+T$	0.009	2.42
O-V^-	chain	0.20	3.5
V^-	G	0.23	1.4
V^-	*Mad*	0.72	1.5
V^-	$Mbc+T$	0.04	1.4
V^-	chain	0.27	3.3

able similarities. The probability density of the defect electron, plotted as a function of the linear distance to the defect under the supposition that these tensors belong to silicon atoms on a [011] zig-zag chain, showed a nearly perfect exponential decay.

The results of the present experiment demonstrate that for the oxygen-vacancy complex a similar group of *Mad* tensors exists. The tensors of this particular group have three features in common: (1) the tensors are all axial with the axial direction very nearly parallel to [111], (2) the second-largest principal value has its direction perpendicular to the *Mad* plane, i.e., perpendicular to the $(0\bar{1}1)$ plane, and (3) the ratios a/b and b/c of the tensors have about the same values. The patterns of the angular dependence of these tensors[18] provide even more convincing pictorial evidence for the similarities. When we plot the electron density, $\eta(r)^2$, for this group of tensors as a function of the distance along the two semi-infinite $\langle 011 \rangle$ directions through the center of the defect, it is found that the densities $\eta(r)^2$ have a nearly perfect exponential decay as well. In Fig. 6 the experimental points and a fit to the function $\eta(r)^2=\eta_0^2\exp(-r/r_0)$ [Eq. (17)] are plotted.

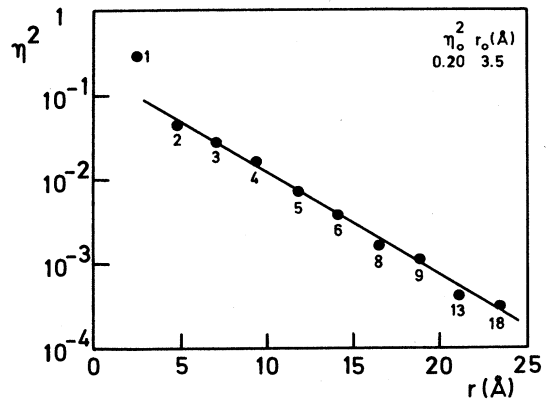

FIG. 6. The localization η^2 of the wave function of the oxygen-vacancy complex as a function of the distance to the center of the defect taken along the [011] chain. The numbers correspond to the *Mad* tensors in Table III. The line is a logarithmic fit to the curve $\eta(r)^2=\eta_0^2\exp(-r/r_0)$, the parameters of which are shown in Table V.

ted. Measured points show only small deviations from the line with $\eta_0^2=0.20$ and $r_0=3.5$ Å. These parameters for O-V^- are included in Table IV, as well as those for V^-. The data for tensor *Mad*1 are not contained in the fit. A reason for the somewhat exceptional position of tensor *Mad*1 may be found in the relatively large lattice distortions for the nearest atoms of the vacancy.

When we compare these results with those for the negative vacancy, we notice that a one-to-one assignment can be made between the *Mad* tensors of O-V^- and V^-. The values $\eta_0^2=0.27$ and $r_0=3.3$ Å for the vacancy are hardly different. This indicates that for both defects the localization of the charge density and its extension through the [011] chain in the *Mad* plane are nearly the same. For comparison, we show in Fig. 7 the tensors of the *Mad* chain with the largest isotropic part, *Mad*1, and with the smallest, *Mad*18 (O-V^-) and *Mad*17 (V^-).

In analogy with the model proposed for the negative vacancy, we thus assign the tensors of the group marked "ch" in Table III to the lattice sites on the zig-zag chains of atoms that lie along the [011] and $[0\bar{1}\bar{1}]$ directions starting at the center of the defect. This suggestion was already made by Watkins and Corbett[10] for the atoms on the sites which they labeled *A*, *B*, and *C* (see Table IV). In this quasi-one-dimensional defect, 81% of the electron density is confined to the chain. Along this chain of atoms the electron density stretches outward over a large distance: in our assumption that the ten *Mad* tensors measure the hyperfine interactions with the first ten atoms along the chain, this distance is farther than 19.2 Å. This is the straight-line distance to the tenth atom along the *Mad* chain, but it constitutes the 53rd shell in the group of all *Mad*-class shells, and there are *even some 1500 atoms within the sphere of this radius.*

Further support for the chain model can be found in theoretical studies performed by Kane.[19] Using a Green's-function method, the charge distribution around a localized impurity in silicon is calculated in up to 72 shells for a midgap state, and in up to 27 shells for three different bound-state energies. It is found that the charge disturbance propagates with a strong preference along similar coplanar atom chains, of which 12 exist in this higher tetrahedral symmetry. Kane argues that his results can be related to the so-called fifth-neighbor interactions, which are of the coplanar angle-angle type. In a lattice with the diamond structure with its strong covalent bonds the linear distance in the lattice between two sites may be less important than the number of "steps" along the bonds between two sites. To reach the site $[\bar{1}33]$ from the center of the defect, one has to take only three bond steps along the [011] chain, while it is the fifth neighbor.

In Refs. 8 and 15, Kane's results have already been plotted in the same manner as in Fig. 6. Although the theoretical results apply to the 12 $\langle 110 \rangle$ chains in a crystal with cubic symmetry and for a very simple potential, it is interesting to note that the extension of the calculated charge density along the chain of atoms, $r_0=3.4$ Å, agrees very well with the extension for our experimental data.

A theoretical calculation specifically on the oxygen-

vacancy complex was performed by Caldas *et al.*,[20] using the multiple-scattering $X\alpha$ method in a 17-atom cluster, i.e., a central oxygen atom surrounded by its 4 nearest and 12 next-nearest neighbors. Although it is obvious that this cluster calculation will never reveal many details on the extended electronic structure of the defect, one of the results suggests a charge concentration in the *ad* plane. When the unpaired electron was accommodated in the b_1^* level, a charge concentration was found on the nearest and next-nearest neighbors that lie around a ⟨110⟩ direction adjacent to the atoms *a* and *d* where the unpaired electron is mainly located. The calculated hyperfine interaction on *a* and *d* was about 800 MHz, nearly a factor of 2 larger than the measured value (~412 MHz). However, a considerable charge concentration was also calculated for the atoms of the first general-class shell. Still, the fact that a charge concentration is found in and close to the {110} plane is consistent with our experiment.

For the vacancy, Sprenger *et al.* also looked for "chainlike" groups of tensors among the other classes.[8,15] Indeed, they succeeded in isolating a group of *G*-class tensors on the following grounds: (1) the largest principal values have their direction nearly parallel to ⟨111⟩ directions, (2) the second-largest principal values have their directions nearly parallel to ⟨101⟩ directions, and (3) the ratios of the LCAO parameters, a/b, are of the same order of magnitude for all of the tensors, as are the ratios b/c. Inspection of Table III reveals that the tensors *G*1, *G*2, *G*4, *G*5, *G*8, *G*9, and *G*11, marked "ch2" for O-V^-

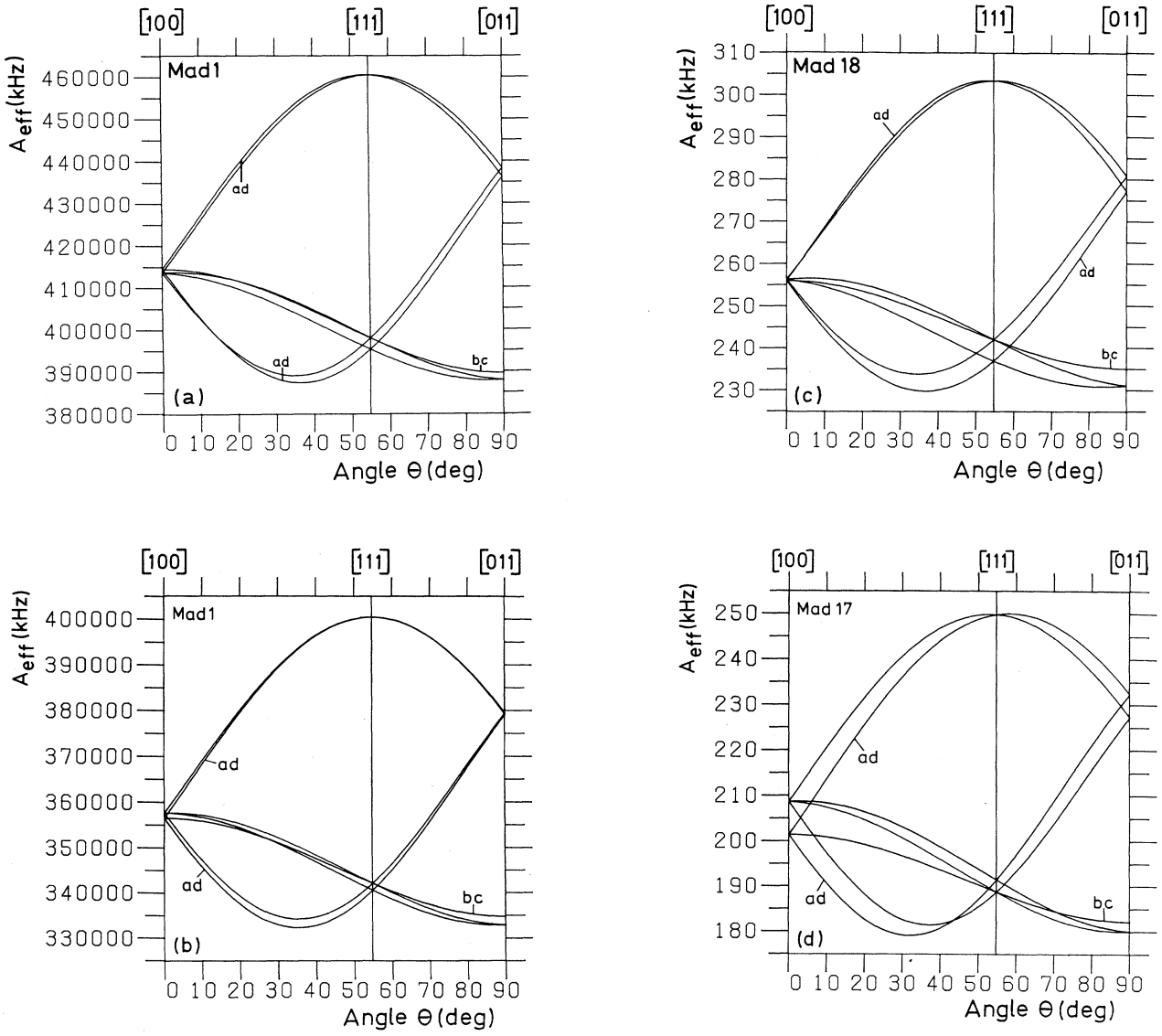

FIG. 7. Hyperfine-interaction tensors for the *Mad* chain of the oxygen-vacancy complex and the vacancy. (a) and (b) for the interactions with the largest isotropic part, *Mad*1, for O-V^- and V^-, respectively; (c) and (d) for the interactions with the smallest isotropic part, *Mad*18 (O-V^-) and *Mad*17 (V^-), respectively.

also meet these criteria. By inspection of Table II, it is seen that the largest principal value alternates its direction between a ⟨111⟩ direction parallel to the *Mad* mirror plane and a ⟨111⟩ direction parallel to the *Mbc* mirror plane. Unfortunately, this sequence seems to be interrupted at *G*8 and *G*9. One can easily argue, however, that only one of these two tensors belongs to the chain. From Table III it can be seen that η^2 decreases roughly by a factor of 2 between successive members of the chain, which is equal to the decay length in the *Mad* chain. Therefore, both of them cannot be a member of the group. On the basis of this argument, *G*8 seems a better choice than *G*9. On the other hand, *G*9 is more similar to the other tensors of the group. Without more detailed knowledge of the spatial extent of the wave function of the defect electron, it is not possible to make a well-founded choice between the two.

An interesting point is the assignment of these tensors to shells. For the vacancy it was observed that the first *G* tensor, *G*1, is very similar to tensor *Mad*4 of the *Mad* chain and, therefore, that lattice position [$\bar{2}$24] was a good candidate for the assignment of *G*1.[8] It was argued that at the position of *Mad*3, [$\bar{1}$33], a part of the electron wave function "branched off," giving rise to a chain of *G* tensors. Inspection of Tables II and III shows that, for O-V^-, the tensors *G*1 and *Mad*4 are also very similar. In Fig. 8 we show the angle-dependent patterns of the tensors *G*1 and *Mad*4 for both defects. We therefore argue that, for the oxygen-vacancy complex, this branching-off mechanism is also present and that it happens at the same lattice site. In view of the importance of the earlier-mentioned fifth-neighbor interaction, and the fact

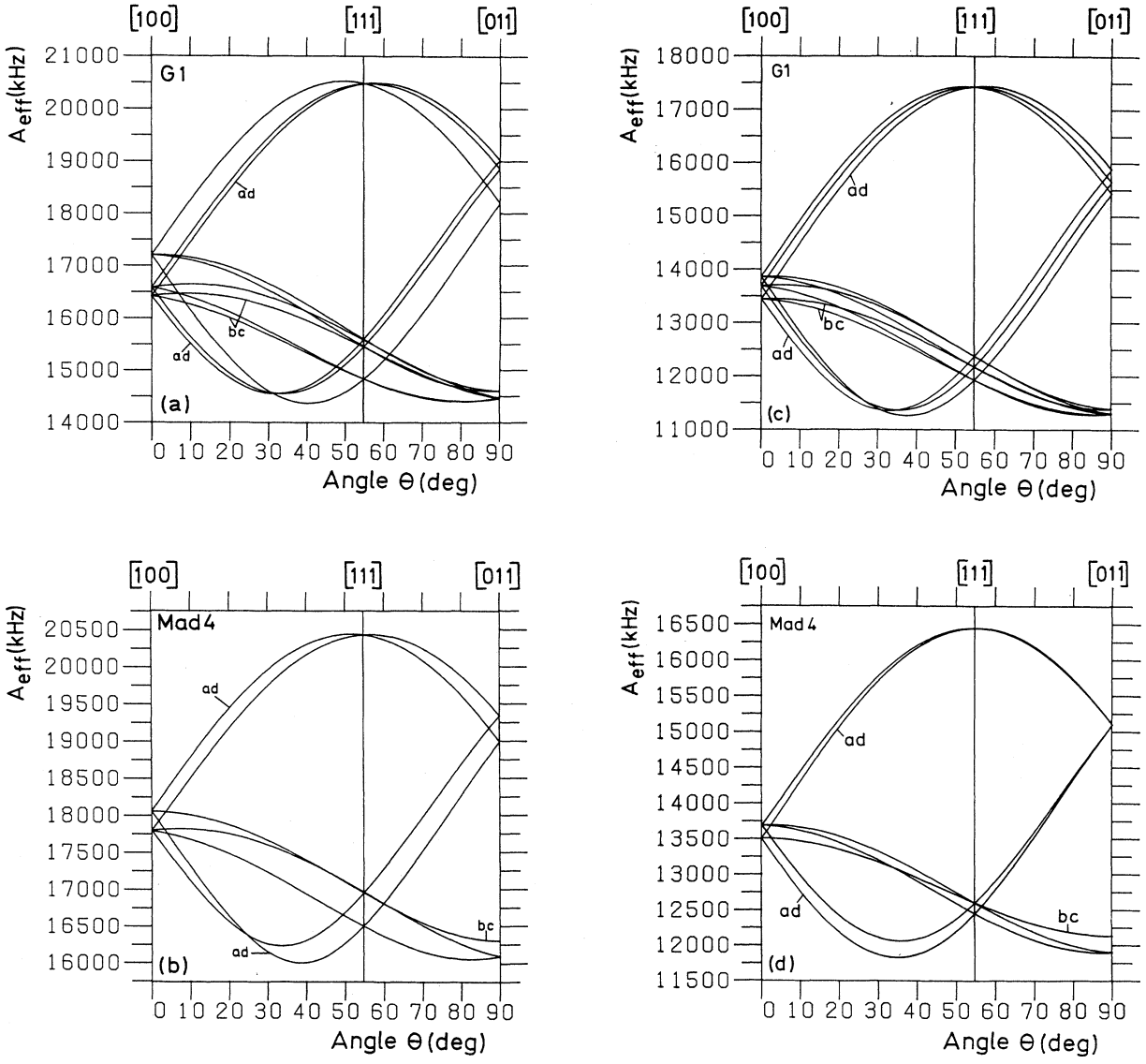

FIG. 8. Angular dependence for the hyperfine interaction tensors *G*1 and *Mad*4 of the oxygen-vacancy complex, (a) and (b), respectively, and the vacancy, (c) and (d), respectively.

that the fifth neighbor of the vacant lattice site is located at $[\bar{1}33]$, this model seems very conceivable. The site assignments as given in Table III for the G-chain tensors are based on this consideration; they should be taken as only tentative.

B. The forbidden plane

In our experiment the existence of a finite contact hyperfine interaction was observed for atoms in the *Mbc* plane, which includes, as a special case, the twofold axis of the defect. The occurrence of this hyperfine interaction cannot be explained by the simple one-electron LCAO model as described in Sec. I D. From Eqs. (10) and (11) it follows that the s part of the electron wave function vanishes for atoms in the *Mbc* plane. Only a nonisotropic contribution from the p part of the wave function is allowed. Also, from the characters of the representation for a b_1 level in the $2mm$ point-group table, this can directly be seen.

Two possible origins for the observed interactions will be discussed: (1) distortion, and (2) many-electron effects and configuration interaction. Also, Lannoo[21] considered these, in response to the first publication of V^- results.[7] Although the treatment of Lannoo is tailored to the problem of the negative vacancy, we think that it is also suited for this case, as the magnitudes of the contact interactions for both the *Mbc* tensors and the T tensor are very much the same.

In the nearest-neighbor, one-electron defect model the spin density of the unpaired electron is localized only on the two neighbors a and d (Fig. 1). The electron is in the state $(a-d)/\sqrt{2}$. For strong displacements one should consider the coupling between the states a_1 and a_1', which is induced by a trigonal Jahn-Teller distortion. As a result, the exact states a_1 and a_1' should be written as

$$a_1=\frac{(b+c)+\lambda(a+d)}{[2(1+\lambda^2)]^{1/2}}\ ,$$
$$a_1'=\frac{\lambda(b+c)-(a+d)}{[2(1+\lambda^2)]^{1/2}}\ . \tag{18}$$

When the trigonal distortion is so large that the $a_1'^*$ level is raised above the b_1^* level, the term $\lambda^2(b+c)^2$ should give rise to a contact hyperfine interaction on the atoms b and c. Lannoo, however, rejected this solution by arguing that the required distortion would be too large to keep λ small, or, in other words, in that case the observed hyperfine interactions should even have been much larger.

The second possibility that was investigated by Lannoo is that of configuration interaction. This interaction is discussed for a system of five electrons that can occupy the ground-state configuration $|\psi_0\rangle=|a_1\bar{a}_1a_1^*\bar{a}_1^*b_1^*\rangle$ and four excited states of the right symmetry. The conclusion of Lannoo is that it is indeed possible to account for a nonvanishing spin density in the *bc* plane. The observed small hyperfine interactions in the forbidden plane, as compared to other neighbor sites, confirm that they should be considered to arise from second-order effects.

C. Dipole-dipole interactions

In this subsection we will take a closer look at the dipole-dipole interaction between an electron and a nuclear spin. This interaction is given in Eq. (14). As shown in Sec. I D for a LCAO wave function constructed from s and p orbitals, one can derive an axially symmetric dipole-dipole tensor $\overleftrightarrow{B}_i$, with principal values as given by Eq. (15). In deriving this expression, we only took into account the p part of the wave function that is centered at the nucleus itself. However, one should also consider contributions from parts of the wave function that are localized on all the other atoms surrounding the nucleus. It is obvious that this is practically impossible. It is not necessary, however, to consider all the surrounding atoms.

In the simplest case of electron spin in a point charge, the dipole-dipole tensor $\overleftrightarrow{B}$ has principal values $(2b_{dd}, -b_{dd}, -b_{dd})$, where

$$b_{dd}=\frac{\mu_0}{4\pi}g\mu_B g_N\mu_N\eta^2R^{-3}\ , \tag{19}$$

with η^2 the fraction of the electron charge and R the distance between the nucleus and the point charge. The tensor has its axial direction along their connection line.

Because of the R^{-3} dependence, this interaction, which arises from spin density on neighbor sites, is usually rather small compared to the interaction with the central p orbital calculated with Eq. (15). This is supported by the numerical factors; while in Eq. (15) $2/5\langle r^{-3}\rangle_p=7.264\times10^{30}\ \mathrm{m}^{-3}$, for nearest neighbors in Eq. (19) $R^{-3}=0.077\times10^{30}\ \mathrm{m}^{-3}$ only. Moreover, η^2 is of considerable magnitude only on the two first neighbors of the vacancy (~0.3 on each). Therefore the dipole-dipole

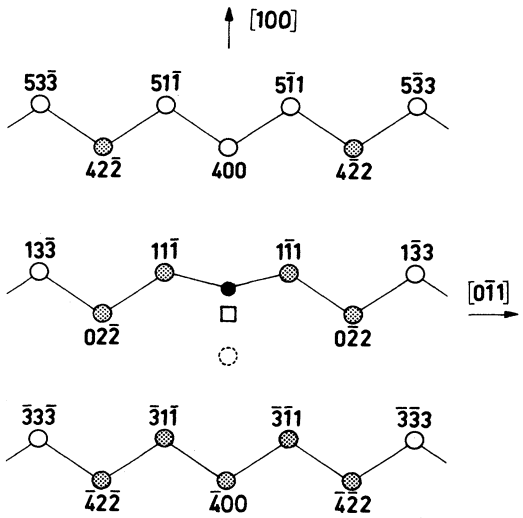

FIG. 9. Part of the symmetry-forbidden (011) plane. Lattice sites for which the hyperfine interaction could be identified from calculated dipole-dipole interactions are shaded. The solid dot is the oxygen atom; the dashed circle indicates where the dangling-bond atoms a and d are located above and below the plane.

interaction due to spin on surrounding nuclei can only be observed if the contribution from the orbital on the site itself, described by Eq. (15), is very small. This situation occurs for the oxygen-vacancy complex for atoms in the "forbidden" plane of the atoms b and c.

As a typical example, we will calculate the dipole-dipole tensor for the atom on the twofold axis through the center of the defect at the position $[\bar{4}00]$. The point charges η^2 are taken to be on the atoms a and d (see Fig. 1). The Cartesian dipole-dipole interaction tensor resulting from a point charge at site $a=[\bar{1}11]$ is

$$\overleftrightarrow{B}=b_{dd}\begin{bmatrix}1.455 & 0.818 & 0.818\\ 0.818 & -0.727 & 0.273\\ 0.818 & 0.273 & -0.727\end{bmatrix}.$$

The dipole-dipole–interaction tensor resulting from the site $d=[\bar{1}\,\bar{1}\,\bar{1}]$ is found by the transformation $m_{(011)}\overleftrightarrow{B}$. Inserting the values $\eta^2=0.2998$ and $R=4.501$ Å into Eq. (19), one finds $b_{dd}=-51.6$ kHz. Adding the two tensors yields

$$\overleftrightarrow{B}=\begin{bmatrix}-149.9 & 0 & 0\\ 0 & 75.0 & -28.2\\ 0 & -28.2 & 75.0\end{bmatrix}\text{ kHz}.$$

This tensor has to be compared with the measured tensor $T1$:

$$\overleftrightarrow{B}=\begin{bmatrix}-164.1 & 0 & 0\\ 0 & 82.1 & -50.0\\ 0 & -50.0 & 82.1\end{bmatrix}\text{ kHz}.$$

As can be seen, the agreement between calculated and measured $\overleftrightarrow{B}$ tensors is quite satisfactory considering the crude approximation of taking point charges instead of

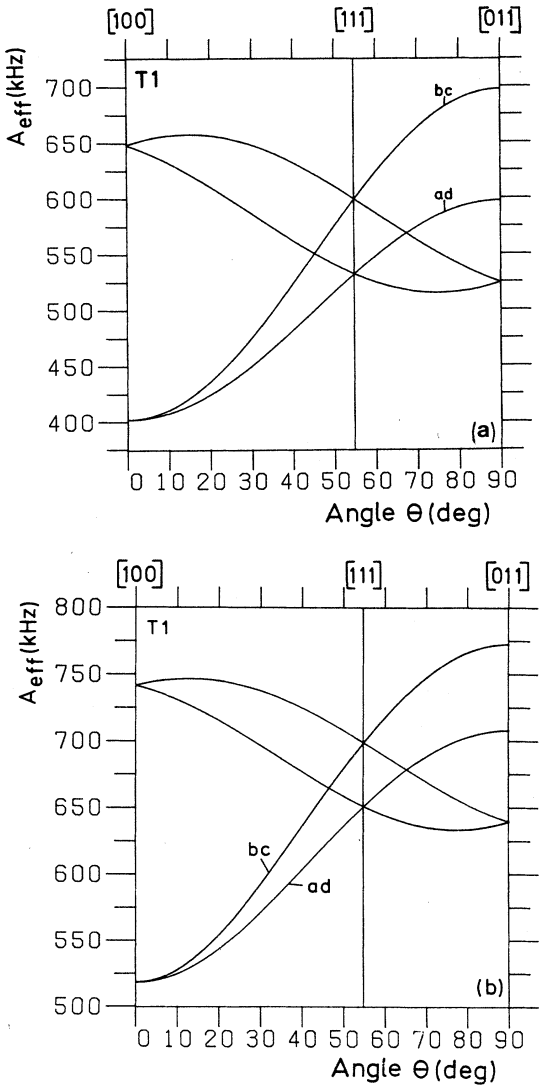

FIG. 10. Angle-dependent patterns for the tensors $T1$ of (a) the oxygen-vacancy complex and (b) the vacancy.

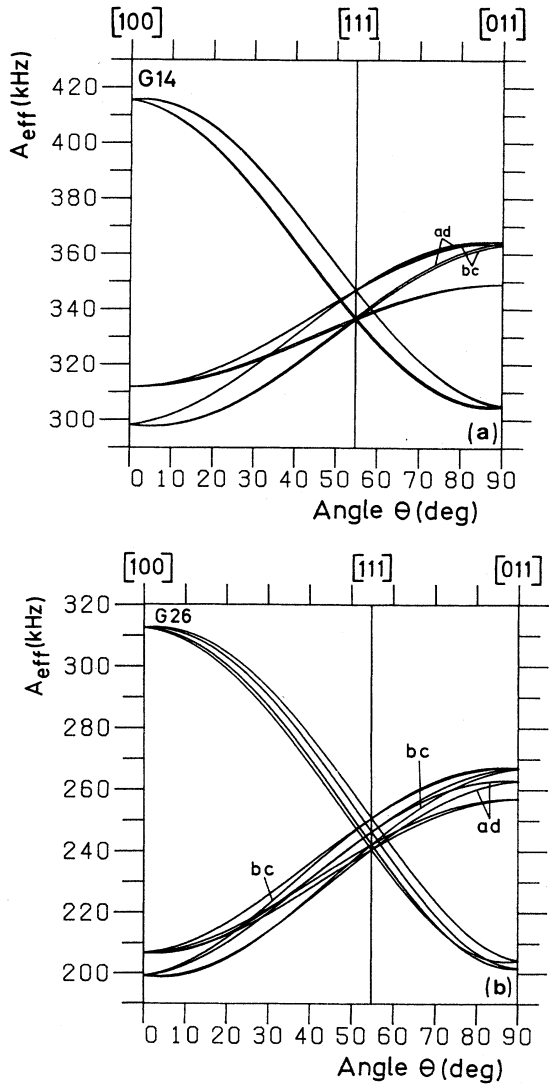

FIG. 11. Angle-dependent patterns for the tensors $G14$ of the oxygen-vacancy complex and $G26$ of the vacancy. Note that both tensors have nearly tetragonal symmetry.

the real orbitals. This means that on site [$\bar{4}00$] the observed hyperfine interaction is largely determined by dipole-dipole interaction, rather than by LCAO admixture.

Within the class of *Mbc* tensors there is one, *Mbc*4, which has about the same principal values as *T*1. Only the axial direction in the (011) plane is rotated over about 70° (or 110°) with respect to *T*1. Inspection of Fig. 9 reveals that a rotation over 110° around the axis of the two point charges at *a* and *d* brings position [$\bar{4}00$] almost exactly at [$0\bar{2}2$]. For tensor *Mbc*4, when assigned to the positions [$02\bar{2}$] and [$0\bar{2}2$], we can thus draw the same conclusions.

Dipole-dipole tensors $\overleftrightarrow{B}$ have further been calculated for sites in these two and various other shells, taking into account charge densities on the nearest neighbors [$\bar{1}11$] and [$\bar{1}\,\bar{1}\,\bar{1}$] and on the next-nearest [022] and [$0\bar{2}\bar{2}$] as well. Localizations for *Mad*1 and *Mad*2 were used as given in Table III. The resulting assignments to hyperfine tensors and calculated values are listed in Table VI. Results for a point-charge approximation are indicated by the entry "pc." Results indicated with "orb" have been calculated using more realistic Slater-type orbitals,[8,22] centered on these four neighbor sites.

As can be seen from Table VI, the match between the experimental and calculated values of tensor *T*1 is very good, if it is accepted that the Fermi-contact interaction is positive, although it should be negative in view of the coefficients in Eq. (13). This is a valuable result, as the position [$\bar{4}00$] is one of the two nearest atom positions on the twofold axis of the defect. The anisotropy of *T*1 can thus entirely be explained as arising from dipole-dipole interactions; the positive contact interaction can qualitatively be understood by the mechanism of exchange core polarization.[23] In Fig. 10 the tensors *T*1 for the oxygen-vacancy complex and the vacancy are shown. It can be seen that the tensors are very similar. This is a further confirmation that these tensors arise almost completely from dipole-dipole interaction, the precise structure of the defect being of minor importance.

The dipole-dipole interaction tensor for the nearest-neighbor sites in the *bc* plane has also been calculated in order to make an assignment with one of the tensors *Mbc*1–*Mbc*6. It is to be expected that either *Mbc*1, the tensor with the largest contact hyperfine interaction, or *Mbc*6, the tensor with the largest anisotropy, would be

TABLE VI. Comparison of calculated dipole-dipole interactions and experimental values for anisotropic hyperfine interactions (in kHz). Expt. denotes the experimental values, pc [*xyz*] are values calculated at site [*xyz*] as a result of point charges at four chain positions, and orb [*xyz*] are values calculated for Slater-type orbitals with parameter values $\alpha_s = 1.87$ and $\alpha_p = 1.60$ (Ref. 22). ϵ is the angle (in deg) between the axial directions of calculated and experimental tensors.

Tensor	B_1	B_2	B_3	ϵ	Remarks
Expt. *T*1	−164.2	32.1	132.1		a=565.7 kHz
	∥[100]	∥[011]	∥[$0\bar{1}1$]		
pc [$\bar{4}00$]	−156.3	46.9	109.4	0.0	
orb [$\bar{4}00$]	−162.6	62.7	99.9	0.0	
Expt. *Mbc*1	−153.1	−227.0	380.1		a=2455.8 kHz
		∥[011]			
pc [$11\bar{1}$]	−184.7	−17.6	202.3	4.5	
orb [$11\bar{1}$]	−257.9	−88.2	346.1	1.5	$\vec{B}_{expt}-\vec{B}_{orb}\sim$[011] axial
Expt. *Mbc*2	66.7	48.4	−115.1		$a=-1237.0$ kHz
		∥[011]			
pc [$\bar{4}2\bar{2}$]	49.3	32.1	−81.4	2.0	
orb [$\bar{4}2\bar{2}$]	46.9	35.3	−82.2	0.0	
Expt. *Mbc*3	−344.5	49.9	294.5		$a=-980.2$ kHz
		∥[011]			
pc [$\bar{3}\,\bar{1}1$]	−213.9	39.2	174.7	11.6	
orb [$\bar{3}\,\bar{1}\,1$]	−255.4	88.3	167.1	8.6	
Expt. *Mbc*4	−142.4	122.9	19.6		$a=-903.3$ kHz
		∥[011]			
pc [$0\bar{2}2$]	−153.9	41.1	112.8	3.1	
orb [$0\bar{2}2$]	−208.8	75.3	133.5	7.0	
Expt. *Mbc*5	−61.1	17.7	43.4		$a=-351.9$ kHz
		∥[011]			
pc [$42\bar{2}$]	−38.2	16.1	22.2	4.8	
orb [$42\bar{2}$]	−45.3	20.3	25.0	4.0	
Expt. *G*14	44.2	30.0	−74.2		$a=-341.8$ kHz
	∼∥[100]	∼∥[00$\bar{1}$]	∼∥[010]		
pc [$\bar{1}15$]	47.0	41.0	−87.9	0.4	
orb [$\bar{1}15$]	45.3	36.7	−81.8	2.0	

good candidates for this site. Comparison with the measured tensors shows that there is no real agreement with any of them, but that *Mbc*1 is the most probable one. If we assume, however, that this dipole-dipole interaction is a known contribution, we can subtract it to see what remains. When the calculated result for Slater orbitals is subtracted from tensor *Mbc*1, a more or less axial interaction results, with its axis approximately parallel to [011]. This can result from the only symmetry-allowed admixture: a *p* orbital along [011]. No other *Mbc* tensor gives any reasonable result in this way. Therefore, we are led to the conclusion that tensor *Mbc*1 should be identified with atoms *b* and *c*. The large (positive) contact interaction must again be understood as exchange core polarization, especially important so close to the oxygen atom in the center of the defect, where the unpaired spin density is highest.

Four other *Mbc*-class tensors, *Mbc*2, *Mbc*3, *Mbc*4, and *Mbc*5, can be matched rather well to the lattice sites $[\bar{4}2\bar{2}]$, $[\bar{3}\,\bar{1}\,1]$, $[0\bar{2}2]$, and $[42\bar{2}]$, respectively. From all these assignments it follows that for most of the neighboring atoms in the forbidden (011) mirror-plane, shown shaded in Fig. 9, the observed anisotropic hyperfine interactions can be largely understood from dipole-dipole interactions alone.

Finally, one general-class tensor, *G*14, can be assigned tentatively to shell $[\bar{1}15]$ in the same way. This tensor has nearly tetragonal symmetry and is very similar to tensor *G*26 of the negative vacancy.[8] In Fig. 11 we show the angle-dependent patterns of both tensors.

D. Comparison of tensors of O-V^- with V^-

In Secs. III A and III C we showed that a number of tensors of O-V^- could be assigned to specific lattice sites, either as forming part of a chain, or after calculation of

TABLE VII. Correspondence of hyperfine tensors of O-V^- and V^-. Lattice-site assignments according to chain or dipole-dipole (dip.-dip.) models are indicated. Several parameters as defined in earlier sections are compared. ϵ_i is the angle (in deg) between the *i*th principal direction of O-V^- and V^- (– is indicated if the direction is symmetry prescribed). Values for angles given in parentheses have no significance in view of the almost perfect axiality of the tensor.

O-V^-	V^-	$a_{\text{O-}V^-}/a_{V^-}$	$b_{\text{O-}V^-}/b_{V^-}$	ϵ_1	ϵ_2	ϵ_3	Model, remarks
*G*1	*G*1	1.23	0.99	2.8	1.1	2.8	chain-2 $[\bar{2}24]$
*G*2	*G*3	1.69	1.33	5.0	1.2	5.0	chain-2 $[\bar{3}35]$
*G*4	*G*6	1.55	1.23	4.1	1.7	4.0	chain-2 $[\bar{4}26]$
*G*5	*G*10	1.36	1.21	4.2	0.6	4.2	chain-2 $[\bar{5}37]$
*G*9	*G*15	1.83	1.30	6.9	0.3	6.9	chain-2 $[\bar{6}28]$
*G*14	*G*26	1.43	1.01	1.8	7.1	7.1	dip.-dip. $[\bar{1}15]$
*Mad*1	*Mad*1	1.16	1.08	1.0	–	1.0	chain $[\bar{1}11]$
*Mad*2	*Mad*2	0.78	0.74	3.4	–	3.4	chain [022]
*Mad*3	*Mad*3	0.86	0.77	4.5	–	4.5	chain $[\bar{1}33]$
*Mad*4	*Mad*4	1.30	0.96	3.7	–	3.7	chain [044]
*Mad*5	*Mad*5	1.01	0.88	2.5	–	2.5	chain $[\bar{1}55]$
*Mad*6	*Mad*6	1.10	0.95	4.1	–	4.1	chain [066]
*Mad*8	*Mad*8	1.06	0.86	4.0	–	4.0	chain $[\bar{1}77]$
*Mad*9	*Mad*12	1.30	1.04	3.6	–	3.6	chain [088]
*Mad*13	*Mad*14	1.03	0.93	3.8	–	3.8	chain $[\bar{1}99]$
*Mad*18	*Mad*17	1.26	1.03	4.6	–	4.6	chain [0 10 10]
*Mbc*1	*Mbc*5	12.0	0.28	9.2	–	9.2	dip.-dip. $[1\bar{1}1]$
*Mbc*2	*Mbc*4	−5.90	1.81	0.1	–	0.1	dip.-dip. $[\bar{4}2\bar{2}]$
*Mbc*3	*Mbc*1	0.47	0.98	8.8	–	8.8	dip.-dip. $[\bar{3}\,\bar{1}\,1]$
*Mbc*4	*Mbc*3	1.09	1.06	1.7	–	1.7	dip.-dip. $[0\bar{2}2]$
*Mbc*5	*Mbc*4	−1.68	0.94	5.7	–	5.7	dip.-dip. $[4\bar{2}2]$
*T*1	*T*1	0.85	1.10	–	–	–	dip.-dip. $[\bar{4}00]$
*G*6	*G*4	0.62	0.93[a]	5.4	10.8	10.8	$b/c \simeq 1$
*G*7	*G*8	0.80	0.90	9.3	9.3	1.0	$b/c \simeq 1.6$
*G*10	*G*7	0.40	1.40	13.4	2.5	13.4	$b/c \simeq 3$
*G*11	*G*17	1.45	0.95	5.4	(19.1)	(21.4)	very good axial $\parallel[1\bar{1}1]$
*G*13	*G*18	1.08	1.10	8.5	(31.1)	(30.5)	very good axial $\parallel[1\bar{1}1]$
*G*16	*G*21	0.99	0.88	2.2	2.2	0.8	$b/c \simeq 2.3$
*G*17	*G*20	0.86	1.64	12.6	14.9	12.6	$\sim[0\bar{1}1]$ axial
*Mad*7	*Mad*10	2.65	0.69	2.7	–	2.7	~[100] axial
*Mad*12	*Mad*18	3.45	1.24	0.7	–	0.7	$b/c \simeq 4$, ~[011] axial
*Mad*16	*Mad*15	0.84	0.86	1.2	–	1.2	very good axial $\parallel[111]$
*Mad*20	*Mad*16	0.51	0.80	5.5	–	5.5	$b/c \simeq 7$, $\sim[2\,\bar{1}\,\bar{1}]$ axial

[a]For choice $|b| < |c|$ (and consequently $a/b > 0$) for V^-

dipole-dipole interactions. Most of them could be assigned to the same lattice sites for which proposals were also made in the case of V^-. A few V^- tensors can now be assigned afterwards because of their similarity with O-V^- tensors. First, tensor *Mbc*3 (V^-) is similar to *Mbc*4 (O-V^-) and matches the calculated dipole-dipole interaction for shell $[0\bar{2}2]$ rather well. Tensor *Mbc*4 (V^-) shows some similarity with both *Mbc*2 and *Mbc*5 (O-V^-). Its experimental values are also in between those calculated for the shells $[\bar{4}2\bar{2}]$ and $[42\bar{2}]$, so that in this case no definitive conclusion can still be drawn.

All these identified tensors, together with their counterparts of V^-, are listed in Table VII. However, among the remaining group of tensors that could not be assigned to particular lattice sites yet, there are a number that show remarkable similarities with hyperfine tensors of V^- too. In particular, among some nonaxial tensors similarities are sometimes striking. This resemblance is most easily seen by comparing their angle-dependent patterns.[15,18] Since these similarities may eventually help in a further improvement of the theoretical understanding of these defects, they have been collected and parametrized in Table VII as well.

The large number of similarities between the hyperfine interactions of V^- and O-V^- indicate that there is a close resemblance between their electronic structures. This means that the most important structural difference between the two defects, the presence of an oxygen atom in the core of O-V^-, hardly influences the extended probability density of the paramagnetic electron. The only hyperfine interactions which have been assigned to the same lattice sites, but exhibit a marked difference, are those for atoms *b* and *c*, *Mbc*5 for V^- and *Mbc*1 for O-V^-. These silicon atoms, however, are the only ones which are directly bonded to the oxygen atom in the case of O-V^-, so that a large difference is very much conceivable. The admixed [011] *p* orbital that resulted from our analysis in Sec. III C, may contribute to this bonding. The bonding will be of π type, as admixture of a similar unpaired [011] *p* orbital is observed on the oxygen atom.[9] For V^- no such bonding is required. Consequently, admixed [011] orbitals are lacking in that case.

IV. CONCLUSIONS

We presented results of a study of the oxygen-vacancy complex in its negatively charged state using electron-nuclear double resonance (ENDOR). The hyperfine interactions between the unpaired defect electron and 50 shells of surrounding atoms have been determined. These shells contain 145 silicon atoms. Since in ENDOR experiments the spatial extension of wave functions is probed, this experiment has yielded very detailed information on the electronic structure of the negative charge state of the oxygen-vacancy complex.

The spin density of the unpaired electron is found to be strongly confined to the $(0\bar{1}1)$ mirror plane of the two dangling-bond neighbor atoms *a* and *d*. About 81% of the spin density is localized in the two semi-infinite chains of atoms that lie zig-zag around the [011] directions through the center of the defect. Along these two [011] chains of atoms, the measured wave function stretches outwards over more than 19 Å. The tensors that measure the hyperfine interactions with the first ten neighbors along these chains are *Mad*1–*Mad*6, *Mad*8, *Mad*9, *Mad*13, and *Mad*18. This assignment is rather reliable, as in experiments for defects like VV^+, VV^-, and V^- similar "chainlike" groups of atoms were found. With V^- there is even a one-to-one correspondence between the *Mad*-class tensors.

A second group of tensors from the *G* class was found to exhibit a similar exponential behavior as the group of *Mad*-chain tensors. The tensors of this group are, apart from a small shift of the isotropic part, very similar to a group of *G*-class tensors that was found for the negative vacancy. For both defects, these "chains" of tensors seem to "branch off" at the site of *Mad*3, $(\bar{1}33)$, and thus give support to the importance of the so-called fifth-neighbor interaction.

On the basis of a comparison of calculated dipole-dipole interactions with experimental values, it was possible to assign seven hyperfine-interaction tensors to particular shells of atoms. All but one of these shells are in the forbidden (011) mirror plane of the neighbors *b* and *c*. The most important and also most reliable assignment was made for tensor *T*1. The assignments of the tensors *T*1, *Mbc*3, *Mbc*4, and *G*14 are, moreover, supported by the fact that, for the vacancy, equivalent tensors could be found. This again is strong proof for the similarity between the two defects. The assignments of the tensors *Mbc*2 and *Mbc*5 are somewhat more tentative.

The studies of V^- and of O-V^- have shown that both defects have in common some very remarkable features that are a direct consequence of their electronic structure. At first sight, it seems a hopelessly complicated task to give a theoretical explanation of the complete electronic structure of these two defects. Yet, our ENDOR studies indicate that it is probably very well possible to deal with some features separately.

[1]G. Bemski, J. Appl. Phys. **30**, 1195 (1959).
[2]G. D. Watkins, J. W. Corbett, and R. M. Walker, J. Appl. Phys. **30**, 1198 (1959).
[3]G. D. Watkins, J. Phys. Soc. Jpn. **18**, Suppl. II, 22 (1963).
[4]G. D. Watkins, in *Radiation Damage in Semiconductors,* edited by P. Baruch (Dunod, Paris, 1965), p. 97.
[5]J. G. de Wit, E. G. Sieverts, and C. A. J. Ammerlaan, Phys. Rev. B **14**, 3494 (1976).
[6]E. G. Sieverts, S. H. Muller, and C. A. J. Ammerlaan, Phys. Rev. B **18**, 6834 (1978).
[7]M. Sprenger, S. H. Muller, and C. A. J. Ammerlaan, Physica B+C **116B**, 224 (1983).
[8]M. Sprenger, S. H. Muller, E. G. Sieverts, and C. A. J. Ammerlaan, Phys. Rev. B **35**, 1566 (1987).
[9]R. van Kemp, M. Sprenger, E. G. Sieverts, and C. A. J. Ammerlaan, this issue, the following paper, Phys. Rev. B **40**, 4054 (1989).
[10]G. D. Watkins and J. W. Corbett, Phys. Rev. **121**, 1001 (1961).

[11]J. R. Morton and K. F. Preston, J. Magn. Reson. **30**, 577 (1978).
[12]E. G. Sieverts and C. A. J. Ammerlaan, in *Radiation Effects in Semiconductors, 1976,* edited by N. B. Urli and J. W. Corbett (The Institute of Physics, London, 1977), p. 213.
[13]E. G. Sieverts, S. H. Muller, and C. A. J. Ammerlaan, Solid State Commun. **28**, 221 (1978).
[14]E. G. Sieverts, Ph.D. thesis, University of Amsterdam, 1978.
[15]M. Sprenger, Ph.D. thesis, University of Amsterdam, 1986.
[16]H. H. Woodbury and G. W. Ludwig, Phys. Rev. **117**, 102 (1960).
[17]G. H. Fuller, J. Phys. Chem. Ref. Data **5**, 835 (1976).
[18]R. van Kemp, Ph.D. thesis, University of Amsterdam, 1988.
[19]E. O. Kane, Phys. Rev. B **31**, 5199 (1985).
[20]M. J. Caldas, J. R. Leite, and A. Fazzio, Physica B+C **116B**, 106 (1983).
[21]M. Lannoo, Phys. Rev. B **28**, 2403 (1983).
[22]C. A. J. Ammerlaan and J. C. Wolfrat, Phys. Status Solidi B **89**, 541 (1978).
[23]D. Ikenberry, A. N. Jette, and T. P. Das, Phys. Rev. B **1**, 2785 (1970).